INTERNATIONAL JOURNAL FOR NUMERICAL METHODS IN FLUIDS
Int. J. Numer. Meth. Fluids 2002; **40**:273–279 (DOI: 10.1002/fld.295)

A new reconstruction scheme for the computation of inviscid compressible flows on 3D unstructured grids

L. A. Catalano*,†

Dipartimento di Ingegneria Meccanica e Gestionale, Centro di Eccellenza di Meccanica Computazionale, Politecnico di Bari, via Re David 200, I-70125, Bari, Italy

SUMMARY

A finite-volume method for the solution of three-dimensional inviscid compressible flows on cell-vertex tetrahedral meshes is proposed. A higher-order-accurate upwind discretization is obtained by using a new linear reconstruction and a standard flux-difference-splitting scheme. The method is validated by computing the subsonic flow in a 90° rectangular elbow with a total pressure gradient imposed at inlet.

KEY WORDS: compressible; unstructured; reconstruction

1. INTRODUCTION

In the last decade, finite-volume upwind schemes for the discretization of the compressible flow equations have reached a remarkable level of accuracy and robustness, which make them suitable for the numerical simulation of three-dimensional complex flows. However, engineering applications often require the analysis of complex geometries, which can be easily discretized by means of unstructured meshes. Most finite-volume methods for unstructured grids proposed to date employ a cell-vertex discretization, since it allows a natural definition of the cell-based flow gradients, which are required both for the higher-order reconstruction and for the discretization of the viscous terms. Using a dual mesh, a gradient-based reconstruction is applied to compute the left and right states of the interface associated to each side; an approximate Riemann solver is then applied to select the proper upwind contributions, see, e.g. References [1–5]. However, to the knowledge of the author, all of the methods for cell-vertex unstructured grids developed so far reconstruct the flow variables using gradients defined in the two nodes, and computed from the gradients in the surrounding cells, see, e.g. Reference [3], where an average between the Hermitian gradients and the central difference on the side itself is used.

*Correspondence to: L. A. Catalano, Dipartimento di Ingegneria Meccanica e Gestionale, Centro di Eccellenza di Meccanica Computazionale, Politecnico di Bari, via Re David 200, I-70125, Bari, Italy.
† E-mail: catalano@poliba.it

Received May 2001
Revised November 2001

Two motivations have suggested to investigate alternative reconstruction schemes: the discretization of viscous flows needs the cell-based gradients only; therefore, all of the approaches outlined above require an additional computation of gradients which are not necessary for viscous flows. Moreover, when reducing to the one-dimensional flow equations there is no correspondence with the standard one-dimensional upwind extrapolation, as it will be shown in the next section. For such a reason, an alternative, much simpler, reconstruction scheme has been recently proposed in References [6, 7], and validated by computing subsonic and transonic inviscid flows in two-dimensional turbine cascades. In particular, References [7, 8] demonstrate its very good shock-capturing properties and consider its extension to two-dimensional laminar and turbulent flows.

This paper proposes the extension of the reconstruction scheme introduced and tested in References [6–8] to the numerical solution of three-dimensional inviscid flows. The next sections will be devoted to the description of the new reconstruction scheme, that will be tested by computing the subsonic flow in a 90° rectangular elbow with a total pressure gradient imposed at inlet.

2. NUMERICAL METHOD

2.1. Governing equations

The governing equations for three-dimensional, compressible, inviscid flows, are written in integral form as

$$\int_V \frac{\partial U}{\partial t}\,\mathrm{d}V = \oint_{\partial V} \mathscr{F}\cdot\boldsymbol{n}\,\mathrm{d}S \tag{1}$$

In Equation (1), $\boldsymbol{n}$ is the inward normal of the contour of V, ∂V, $U=(\rho,\rho u,\rho v,\rho w,\rho e^0)^{\mathrm{T}}$ is the vector of the conservative variables and $\mathscr{F}\cdot\boldsymbol{n}=[(\rho v_n),(\rho u v_n+pn_x),(\rho v v_n+pn_y),(\rho w v_n+pn_z),(\rho h^0 v_n)]^{\mathrm{T}}$ is the flux entering through the unit element of ∂V. As usual, ρ is the density, p is the pressure, e° is the total internal energy and h° is the total enthalpy. Moreover, $\boldsymbol{v}$ denotes the velocity vector, with normal component $v_n=\boldsymbol{v}\cdot\boldsymbol{n}$ and with Cartesian components u, v and w. The system of governing equations is closed by considering a perfect gas.

2.2. Reconstruction scheme

For clarity and without loss of generality, the description of the space discretization and of the reconstruction scheme will be partly referred to two dimensions. The domain is discretized by means of an unstructured grid composed of triangles (tetrahedra in 3D) with unknowns located at each cell-vertex. The finite volume associated to each internal node i is constructed by intersecting the medians of all surrounding triangles (median planes of all surrounding tetrahedra in 3D), see Figure 1. This allows to associate an interface (ij) to the side connecting the node i with each sorrounding node j. A higher-order-accurate upwind discretization of the Euler equations is then obtained as follows: a left state and a right state, $Q^{\mathrm{L}}_{(ij)}$ and $Q^{\mathrm{R}}_{(ij)}$, are reconstructed on the two sides of the interface (ij) as

$$Q^{\mathrm{L}}_{(ij)} = Q_j + (\nabla Q)_{ji}\cdot\boldsymbol{l}_{ji} \tag{2}$$

$$Q^{\mathrm{R}}_{(ij)} = Q_i + (\nabla Q)_{ij}\cdot\boldsymbol{l}_{ij} \tag{3}$$

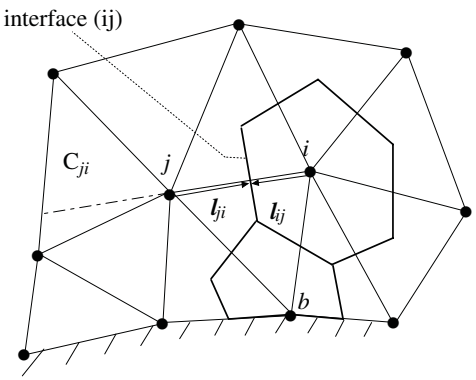

Figure 1. Construction of the dual mesh in two dimensions and determination of the cell C_{ji}.

$\boldsymbol{l}_{ji}$ and $\boldsymbol{l}_{ij}$ being the two opposite vectors pointing from the two nodes i and j to the mid-point of the side, see Figure 1. Standard one-dimensional limiters can also be applied straightforwardly.

Different definitions of the gradients characterize the numerical methods cited in the Introduction, but all of them appear cumbersome and in contrast with the corresponding one-dimensional upwind scheme. Consider a one-dimensional uniform grid: on the interface $(k+1/2)$, $Q^{\mathrm{L}}_{k+1/2}$ is linearly reconstructed as

$$Q^{\mathrm{L}}_{k+1/2} = \tfrac{3}{2}Q_k - \tfrac{1}{2}Q_{k-1} = Q_k + \tfrac{1}{2}(Q_k - Q_{k-1}) \tag{4}$$

Equation (4) shows that in one dimension the reconstruction of the left state (similar arguments hold for the right state) is based on the *gradient* of Q in the left-neighbouring cell, rather than on the *gradient* defined in the node k. Similarly, in two and three dimensions, a unique left-neighbouring cell can be defined as the cell C_{ji} which contains the prolongation of the side (ji), plotted as a dot-dashed line in Figure 1. The cell C_{ji} is searched only once and then stored as a pointer, except in the case of moving grids. The choice of a cell-vertex triangular (tetrahedral in 3D) grid allows to compute the cell-based gradient $(\boldsymbol{\nabla} Q)_{ji} \equiv (\boldsymbol{\nabla} Q)_{C_{ji}}$ uniquely. All of the gradients must be computed once at each iteration, stored, and then used without any additional averaging. For this reason, and since the same gradients must be computed anyway when solving the Navier–Stokes equations, we claim that the proposed higher-order reconstruction minimizes the computational time required for the evaluation of the flow gradients.

It is noteworthy that if the prolongation of the side (ji) lies on a face (or a side in 3D) separating two (or more in 3D) cells, the choice of the cell C_{ji} is not crucial, since only the projection of the gradient onto the side (ji) is used in Equation (2). Obviously, $(\boldsymbol{\nabla} Q)_{ji} \cdot \boldsymbol{l}_{ji}$ is continuous (its derivatives are not) through each face. In the case of moving grids, one can move from one cell to another one continuously, as well.

The flux-difference-splitting of Roe [9] is then used to solve the Riemann problem defined at each interface. The flux $\mathscr{F}_n = \boldsymbol{\mathscr{F}} \cdot \boldsymbol{n}$ is computed as

$$\mathscr{F}_n = \boldsymbol{\mathscr{F}} \cdot \boldsymbol{n} = \frac{\mathscr{F}_n^{\mathrm{L}} + \mathscr{F}_n^{\mathrm{R}} - \delta\mathscr{F}_n}{2} \tag{5}$$

so as to select the upwind contributions by means of the term $\delta\mathscr{F}_n$. In three dimensions, one has:

$$\delta\mathscr{F}_n = \sum_{k=1}^{5} \alpha_k |\lambda_k| \boldsymbol{e}_k \tag{6}$$

In Equation (6), $\alpha_k,\ k=1,\ldots,5$, are the intensities of the entropy, of the shear and of the acoustic waves, and $\lambda_k,\ k=1,\ldots,5$, are the corresponding propagation velocities:

$$\begin{aligned}
&\alpha_1 = \delta\rho - \frac{\delta p}{\tilde{c}^2}, && \lambda_1 = \tilde{v}_n \\
&\alpha_2 = \tilde{\rho}\delta v_s, && \lambda_2 = \tilde{v}_n \\
&\alpha_3 = \tilde{\rho}\delta v_t, && \lambda_3 = \tilde{v}_n \\
&\alpha_4 = \frac{\delta p + \tilde{\rho}\tilde{c}\delta v_n}{2\tilde{c}^2}, && \lambda_4 = \tilde{v}_n + \tilde{c} \\
&\alpha_5 = \frac{\delta p - \tilde{\rho}\tilde{c}\delta v_n}{2\tilde{c}^2}, && \lambda_5 = \tilde{v}_n - \tilde{c}
\end{aligned} \tag{7}$$

$v_s = \boldsymbol{v}\cdot\boldsymbol{s}$ and $v_t = \boldsymbol{v}\cdot\boldsymbol{t}$ being two tangential components of the velocity vector ($\boldsymbol{s}\times\boldsymbol{t} = \boldsymbol{n}$). Finally, $\boldsymbol{e}_k,\ k=1,\ldots,5$, are the eigenvectors which project each wave contribution onto the conservative variable vector:

$$\begin{aligned}
\boldsymbol{e}_1 &= (1, \tilde{u}, \tilde{v}, \tilde{w}, |\tilde{\boldsymbol{v}}|^2/2)^{\mathrm{T}} \\
\boldsymbol{e}_2 &= (0, s_x, s_y, s_z, \tilde{v}_s)^{\mathrm{T}} \\
\boldsymbol{e}_3 &= (0, t_x, t_y, t_z, \tilde{v}_t)^{\mathrm{T}} \\
\boldsymbol{e}_4 &= (1, \tilde{u} + n_x\tilde{c}, \tilde{v} + n_y\tilde{c}, \tilde{w} + n_z\tilde{c}, \tilde{h}^\circ + \tilde{c}\tilde{v}_n)^{\mathrm{T}} \\
\boldsymbol{e}_5 &= (1, \tilde{u} - n_x\tilde{c}, \tilde{v} - n_y\tilde{c}, \tilde{w} - n_z\tilde{c}, \tilde{h}^\circ - \tilde{c}\tilde{v}_n)^{\mathrm{T}}
\end{aligned} \tag{8}$$

In Equations (7) and (8), $\delta() = ()_{\mathrm{R}} - ()_{\mathrm{L}}$, and $\tilde{}$ denotes the Roe averages:

$$\begin{aligned}
\tilde{\rho} &= \sqrt{\rho_{\mathrm{L}}}\sqrt{\rho_{\mathrm{R}}} \\
\tilde{\boldsymbol{v}} &= \frac{\boldsymbol{v}_{\mathrm{L}}\sqrt{\rho_{\mathrm{L}}} + \boldsymbol{v}_{\mathrm{R}}\sqrt{\rho_{\mathrm{R}}}}{\sqrt{\rho_{\mathrm{L}}} + \sqrt{\rho_{\mathrm{R}}}} \\
\tilde{h}^\circ &= \frac{h^\circ_{\mathrm{L}}\sqrt{\rho_{\mathrm{L}}} + h^\circ_{\mathrm{R}}\sqrt{\rho_{\mathrm{R}}}}{\sqrt{\rho_{\mathrm{L}}} + \sqrt{\rho_{\mathrm{R}}}} \\
\tilde{c} &= (\gamma - 1)(\tilde{h}^\circ - |\tilde{\boldsymbol{v}}|^2/2)
\end{aligned} \tag{9}$$

2.3. Reconstruction near boundaries and boundary conditions

When a face lies on a boundary, the dual mesh is completed by using the boundary itself, see the boundary node b in Figure 1. The flux through each boundary face is computed directly by means of the values in the boundary nodes; in particular, when b is on a solid wall, the pressure forces must be added to the momentum equation, only.

The lack of further cells beyond the boundaries makes it impossible to apply the higher-order reconstruction onto the near-boundary interfaces. The reduced accuracy is negligible for far-field boundaries, where gradients must be very small, but a significant amount of numerical entropy would be generated near solid walls. A simple procedure to overcome this problem has been proposed in Reference [6], following the approach of Reference [10]: a row of auxiliary cells is introduced beyond the solid walls and the states in the auxiliary nodes are updated by imposing the isentropic simple radial equilibrium at the mid-point of each solid face. Here, a similar, but more general approach, which avoids the generation of auxiliary cells, is proposed: when the search of the cell C_{ji} which contains the prolongation of the side (ji) is unsuccessful, the vector $\boldsymbol{l}_{ij}$ is reflected on the solid wall and a new search is started, which surely will be completed successfully. The corresponding cell C_{ji} is pointed with a minus sign, so as to remember that it has been found with a reflected vector. When the cell C_{ji} is invoked with a minus sign in the reconstruction phase, its gradient is modified according to the equations of isentropic simple radial equilibrium. The extension to viscous flows is straightforward.

Finally, the standard characteristic approach is applied to the residuals in the inlet and outlet nodes, to enforce the corresponding boundary conditions.

2.4. Time integration

The state in each node is updated by means of a two-stage Runge–Kutta explicit scheme with non-optimal coefficients 0.42 and 1 and CFL number 0.3.

3. RESULTS

The proposed numerical method has been tested versus the well-known Stanitz elbow flow problem. The employed tetrahedral mesh which discretizes half the symmetric domain has been generated by subdividing each cell of a $56 \times 24 \times 24$ (uniform) structured grid in five tetrahedra, so as to allow the comparison both with the reconstruction scheme of Reference [3] and with the fluctuation splitting method for structured grids proposed in Reference [12].

A total-pressure gradient is imposed at the inlet section of the 90° rectangular elbow, with outlet isoentropic Mach number $M_{2,is} = 0.45$. Figure 2 shows the contours of total-pressure loss, defined as $\Delta p^\circ = (p_1^\circ - p^\circ)/(p_1^\circ - p_2)$, 1 and 2 being the inlet and outlet sections, respectively, and p_1° being the inlet total pressure in the core flow. Since in the low-speed region the centrifugal force is not balanced by the pressure gradient imposed by the streamline curvature in the core, a secondary flow develops along the channel: the convection of the low-total-pressure particles rolls up the initial profile, see Figure 2, which also provides the total-pressure-loss contours at the outlet section, computed by using the present reconstruction scheme. This result is very similar to those obtained by using the other two methods (not shown). In order to analyse if small discrepancies exist, Figure 3 shows the distributions of the pressure coefficient $c_p = (p - p_2)/(p_1^0 - p_2)$ on the suction side ($0 \leqslant s \leqslant 1$), on the end-wall ($1 \leqslant s \leqslant 2$) and on the pressure side ($2 \leqslant s \leqslant 3$), at three axial locations ($s = 0$ and 3 are on the upper symmetry plane). Symbols refer to the experimental results provided in Reference [11], where the inlet total-pressure gradient has been created by inserting a spoiler. Clearly, the formation of the secondary flow is mostly due to the velocity gradient imposed at the inlet;

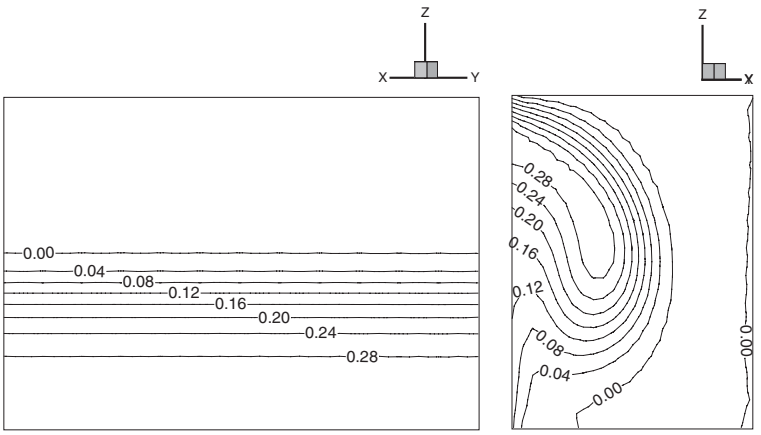

Figure 2. Total-pressure-loss contours at the inlet and outlet sections.

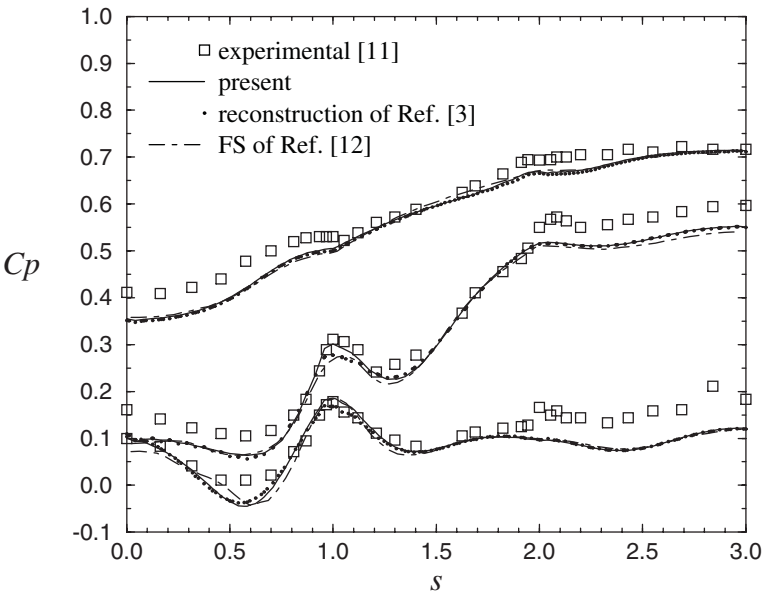

Figure 3. Pressure coefficient distributions at three axial locations.

however, important viscous effects are still present and affect the pressure field. Moreover, uncertainties in the pressure-probe locations on the pressure side ($2 \leqslant s \leqslant 3$) are declared in Reference [11]. Figure 3 reports also the present numerical results, as solid lines, together with those obtained (on the same grid) by using the reconstruction of Reference [3] (dotted lines) and the fluctuation splitting method for structured grids of Reference [12] (dot-dashed lines). For all of them, the comparison with the experimental data shows major discrepancies on the upper part of the suction side ($s \to 0$), due to the presence of important viscous effects and of

lower intensities of the secondary flow. On the contrary, the convective effects dominate the region strongly swept by the vortex, namely the lower part of the suction side ($s \approx 1$), and a better agreement with the experimental data is possible. Obviously, the major discrepancies among the three numerical solutions are found in this high-gradient region. In particular, the present numerical method is capable of reproducing the peaks of c_p slightly better than the reconstruction of Reference [3].

4. CONCLUSIONS

A finite-volume method for the solution of three-dimensional inviscid compressible flows on cell-vertex tetrahedral meshes is presented. In particular, a new higher-order reconstruction of the flow variables is proposed, which involves only the cell-based gradients that will be required anyway for the solution of the Navier–Stokes equations. The numerical method is validated by computing the subsonic flow in a 90° rectangular elbow with total pressure gradient imposed at inlet. The comparison with experimental data and with the numerical results obtained by using both a more cumbersome reconstruction scheme and a fluctuation splitting method demonstrates the accuracy of the proposed technique.

ACKNOWLEDGEMENTS

This research has been supported by ASI (Agenzia Spaziale Italiana) and MIUR (Ministero dell'Istruzione, dell'Università e della Ricerca).

REFERENCES

1. Barth TJ. On unstructured grids and solvers. In *Lecture Series 1990-04*. Von Karman Institute: Belgium, 1990.
2. Barth TJ. Aspects of unstructured grids and finite-volume solvers for the Euler and Navier–Stokes equations. In *Lecture Series 1991-06*. Von Karman Institute: Belgium, 1991.
3. Mohamadi B. Complex turbulent flows computation with a two-layer approach. *International Journal for Numerical Methods in Fluids* 1992; **15**:747–771.
4. Selmin V, Formaggia L. Unified construction of finite element and finite volume discretizations for compressible flows. *International Journal for Numerical Methods in Engineering* 1996; **39**:1–32.
5. Hallo L, Le Ribault C, Buffat M. An implicit mixed finite-volume-finite-element method for solving 3D turbulent compressible flows. *International Journal for Numerical Methods in Fluids* 1997; **25**:1241–1261.
6. Catalano LA. A higher-order-accurate upwind method for 2D compressible flows on cell-vertex unstructured grids. *2nd International Symposium on Finite Volumes for Complex Applications.* Duisburg, Germany, July 19–22, 1999.
7. Catalano LA. A higher-order-accurate reconstruction for the computation of compressible flows on cell-vertex triangular grids. In *Godunov Methods*: *Theory and Applications*, Toro EF (ed). Kluwer Academic/Plenum Publishers: Dordrecht, 2001.
8. Catalano LA. New reconstruction schemes for turbulent compressible flows on unstructured grids. *AIAA Paper 2001–2598,* 2001.
9. Roe PL. Characteristic based schemes for the Euler equations. *Annual Review of Fluid Mechanics* 1986; **18**:337–365.
10. Dadone A, Grossman B. Surface boundary conditions for the numerical solution of the Euler equations. *AIAA Journal* 1994; **32**(2):285–293.
11. Kreatsoulas JC, Lee D, Ballantyne A. Experimental/computational study of viscous flow in an accelerating, 90 degree, rectangular elbow. *AIAA Paper 88-0186*, 1988.
12. Catalano LA. A semi-staggered residual distribution method for 2- and 3-D steady inviscid compressible flows. In *Numerical Methods for Fluid Dynamics V*. Clarendon Press: Oxford, 1995; 225–231.

